

## PAIR MULTIPLICITIES AND PULSAR DEATH

JOHANN A. HIBSCHMAN<sup>1,2</sup>

AND

JONATHAN ARONS<sup>1,2,3</sup>University of California, Berkeley<sup>4</sup>*Draft version October 28, 2018*

## ABSTRACT

Through a simple model of particle acceleration and pair creation above the polar caps of rotation-powered pulsars, we calculate the height of the pair-formation front (PFF) and the dominant photon emission mechanism for the pulsars in the Princeton catalog. We find that for most low- and moderate-field pulsars, the height of the pair formation front and the final Lorentz factor of the primary beam is set by nonresonant inverse Compton scattering (NRICS), in the Klein-Nishina limit. NRICS is capable of creating pairs over a wide range of pulsar parameters without invoking a magnetic field more complicated than a centered dipole, although we still require a reduced radius of curvature for most millisecond pulsars. For short-period pulsars, the dominant process is curvature radiation, while for extremely high-field pulsars, it is resonant inverse Compton scattering (RICS). The dividing point between NRICS dominance and curvature dominance is very temperature-dependent; large numbers of pulsars dominated by NRICS at a stellar temperature of  $10^6$  K are dominated by curvature at  $10^5$  K.

Our principle result is a new determination of the theoretical pulsar death line. Proper inclusion of ICS allows us to reach the conclusion that all known radio pulsars are consistent with pair creation above their polar caps, assuming steady acceleration of a space charge limited particle beam. We identify a new region of the  $P-\dot{P}$  diagram where slow pulsars with narrow radiation beams should be found in sufficiently large surveys.

We also show that the injection rate of electrons and positrons into the Crab Nebula inferred from the polar cap pair creation model at the present epoch ( $10^{39}$  electrons and positrons per second) suffices to explain the nebular X- and  $\gamma$ -ray emission, the best empirical measure of the instantaneous particle loss rate from any pulsar, but that the contemporary injection rate is about a factor of 5 below the rate averaged over the Nebula's history required to explain the Nebular radio emission (assuming the Nebular radio source is homogeneous). It is not clear whether this discrepancy can be resolved by evolutionary effects and by better treatment of nebular inhomogeneity, or is an indication of another particle source in the pulsar's magnetosphere.

*Subject headings:* Acceleration of particles—pulsars: general

## 1. INTRODUCTION

The region above the polar caps of rotation-powered pulsars has long been the focus of research. From the first, e.g. Goldreich & Julian (1969), theoretical papers have centered on the idea that a beam of electrons (or ions) is accelerated up from the polar cap by the electric potential induced by the rotation of the pulsar's intense magnetic field. Shortly afterwards, Sturrock (1971) suggested that this particle beam will emit high-energy gamma-rays via curvature radiation, which will then interact with the background magnetic field and generate copious numbers of electron-positron pairs, forming a pair plasma. Ruderman & Sutherland (1975) suggested that this plasma, once formed, will act to short out the potential, preventing further acceleration. Arons & Scharlemann (1979) then showed that this scenario can occur even when the star freely emits the particle beam.

This basic model has remained qualitatively unchanged for the past 25 years. Recently, however, two important alterations have been made to the theory. First, the importance of general relativistic frame dragging in the creation of the accelerating potential was discovered by Muslimov & Tsygan (1990, 1992) and later elaborated by Muslimov & Harding (1997). Second, several authors (Sturmer, et al. 1995; Luo 1996; Zhang, et al. 1997) have suggested that inverse Compton scattering (ICS) is an important, perhaps the dominant, high-energy photon emission mechanism, rather than the curvature radiation proposed by the earlier theories. Zhang & Harding (2000) used a model of a Compton-dominated pulsar including the GR acceleration to obtain predictions for the emitted gamma-ray spectrum but did not discuss the pair-production rate itself in any detail.

The dominant emission mechanism and accelerating po-

<sup>1</sup> Theoretical Astrophysics Center<sup>2</sup> Physics Department<sup>3</sup> Astronomy Department<sup>4</sup> Address correspondence to J. A. Hirschman, Astronomy Dept., 601 Campbell Hall, U.C., Berkeley 94720-3411; email: [jhirschman@astron.berkeley.edu](mailto:jhirschman@astron.berkeley.edu)

tential combine to set the height of the pair formation front (PFF), the point above the polar cap where enough pairs have been formed to halt any further acceleration of the beam. Given the potential, the PFF height sets the final Lorentz factor of the beam, determining the energy budget of the polar-cap region.

This paper calculates, in a direct analytic manner, and for an arbitrary pulsar, the height of the PFF in the presence of the Muslimov and Tsygan accelerating potential and including the effects of inverse Compton scattering.

Qualitatively, two rates combine to position the PFF: the creation rate of photons capable of pair-producing and the rate at which those photons can pair-produce. Section 2 discusses the approximations used for the pair-production process, Section 3 discusses the emission rate of convertible photons due to various emission mechanisms, Section 4 explains the model of the accelerating potential used, and Section 5 calculates the resultant PFF height.

For simplicity, for the rest of this paper we express all energies and temperatures in units of the electron energy,  $m_e c^2 = 511 \text{ keV} = 5.9 \times 10^9 \text{ K}$ , unless otherwise specified.

## 2. PAIR PRODUCTION

The photons capable of pair-producing in the background dipole magnetic field are those with energy greater than a critical value,

$$\epsilon_a = \frac{32 B_q}{3 B} \frac{\rho_e}{r_e \ln \Lambda} = 2166 B_{12}^{-1} P^{1/2} r_6^{-1} f_\rho \quad (1)$$

where  $B$  is the local magnetic field,  $B_q$  is the critical magnetic field,  $B_q = 4.41 \times 10^{13} \text{ G}$ ,  $r_e$  is the radius of the emission point as measured from the center of the magnetic dipole,  $\rho_e$  is the radius of curvature of the magnetic field at  $r_e$ , and  $\ln \Lambda$  is treated as a constant parameter, here  $\ln \Lambda = 20$  (Arons & Scharlemann 1979). The numerical value expresses the magnetic field in units of  $10^{12}$  Gauss,  $B = 10^{12} B_{12} \text{ G}$ , and assumes that the emission point is at  $r_e = 10^6 r_6 \text{ cm}$  and that the radius of curvature is a factor  $f_\rho$  times the radius of curvature of a dipole field on the last closed field line,  $\rho_e = f_\rho \rho_B$ ,  $\rho_B = 4R_*/3\theta_c = 9.2 \times 10^7 P^{1/2} \text{ cm}$ , where  $P$  is the pulsar spin period. The expected possible range of  $f_\rho$  is from  $f_\rho = 0.011 P^{-1/2}$ , for an extreme multipole field with radius of curvature equal to the stellar radius, to  $f_\rho = 1$ , for a standard dipole field.

These photons (with  $\epsilon > \epsilon_a$ ) must propagate through the magnetic field for a distance

$$\Delta s = \frac{1}{4} \frac{\epsilon_a}{\epsilon} \frac{r_e}{R_*}, \quad (2)$$

in units of the stellar radius  $R_*$  before they pair-produce. Since the pair-production opacity is a sharply increasing function of distance, essentially all such photons pair-produce at this distance. This approximation is best for low- and mid-range field strengths, where  $B < B_q/3$ . At higher fields, not only does the opacity increase more gradually with distance, but other physical processes, such as photon splitting (Harding, et al. 1997), may become important. Most observed pulsars are in the lower regime of magnetic field.

The created pair will be in a high Landau level and will therefore emit synchrotron radiation, bleeding off the com-

ponent of its momentum perpendicular to the local magnetic field. The synchrotron photons with energies above  $\epsilon_a$  then pair-produce themselves, initiating a cascade.

The total number of pairs produced by this cascade may be found by using a modified version of the generational model due to Tadamaru (1973). Each generation of pair production and subsequent synchrotron emission lowers the maximum energy of the photon spectrum by a factor of  $\ln \Lambda$  (Arons & Scharlemann 1979). Since the expected synchrotron number spectrum due to one photon has a power-law index of  $\nu = -3/2$ , the energy is concentrated in the high-frequency end of the spectrum, and we may treat all the photons of the  $i^{\text{th}}$  generation as having energy  $\epsilon_i = \epsilon_{i-1}/\ln \Lambda$ . If there is no energy loss between successive generations, this produces a final pair multiplicity  $M(\epsilon_0) = \epsilon_0/\epsilon_a$  from an initial photon of energy  $\epsilon_0$ .

However, even in the best case, this overestimates the pair production, since a significant fraction of the penultimate generation of pairs will have energies less than  $\epsilon_a$  and will thereby be lost. Given the power-law index of  $\nu = -3/2$ , this reduces the number of photons available to the last generation by a factor of  $\sqrt{\ln \Lambda}$ , giving a single-photon pair multiplicity of

$$M(\epsilon_0) = 1 + \frac{1}{\sqrt{\ln \Lambda}} \frac{\epsilon_0}{\epsilon_a}, \quad (3)$$

namely the sum of the single pair generated by the primary photon and those generated by the cascade.

This pair production cascade does not take place instantaneously; it gradually develops over the distance of  $r_e/4$  it takes the lowest energy convertible photons to pair produce. Most pair production is initiated by photons emitted close to the surface of the star, so  $r_e/R_* \approx 1$  and the length of the cascade is simply  $R_*/4$ . Over this span, the pair production rate is linear with distance. Each successive generation multiplies the number of generated pairs, but it does so over a similarly multiplied propagation distance.

The multiplicity of pairs produced before a height  $s$  by a single photon of energy  $\epsilon$  emitted at height  $s_e$  then has two parts. First, as long as the primary photon has enough distance to pair produce, i.e.  $s - s_e > \epsilon_a/4\epsilon$ , at least one pair will be generated. Second, the cascade of secondaries produced by that pair will generate  $\epsilon/(\epsilon_a \sqrt{\ln \Lambda})$  more pairs, reduced by the fraction of the full  $R_*/4$  available to pair-produce:

$$M(s, s_e, \epsilon) = 1 + \frac{4}{\sqrt{\ln \Lambda}} \frac{\epsilon}{\epsilon_a} (s - s_e) \quad (4)$$

This assumes that  $s - s_e < 1/4$  and ignores the change in the magnetic field through the cascade. Since the magnetic field decreases with height above the polar cap, this on-the-spot approximation slightly over-estimates the amount of pair creation, but it does so consistently for all of the emission mechanisms considered, and so should not change the qualitative results. The quality of these approximations will be discussed in a subsequent paper.

## 3. EMISSION

The rate at which these photons are produced depends on the emission mechanism. There are three primary emission mechanisms which are important over pulsar polar

caps: curvature radiation, resonant inverse Compton scattering (RICS), and nonresonant inverse Compton scattering (NRICS) in both the Thomson and Klein-Nishina regimes.

Each of these mechanisms produces its own characteristic radiation spectrum. However, since all of these spectra are roughly power-laws harder than  $\dot{N}(\epsilon) \propto \epsilon^{-1}$  until truncated at some mechanism-dependent maximum energy, most of the emitted energy is concentrated in photons with energy near this maximum. We then approximate the spectra by assuming that the entire emitted power is converted into photons at the maximum energy, so  $\dot{N}(\epsilon) = P_X/\epsilon_X$ , where  $P_X$  is the power emitted and  $\epsilon_X$  the characteristic energy of an emission mechanism  $X$ .

The characteristic maximum energies of these mechanisms are

$$\epsilon_{NR}^{Th} = 2\gamma^2 T \Delta\mu \quad (5)$$

$$\epsilon_{NR}^{KN} = \gamma \quad (6)$$

$$\epsilon_R = 2\gamma\epsilon_B \quad (7)$$

$$\epsilon_C = \frac{3}{2} \frac{\lambda_C}{\rho} \gamma^3 \quad (8)$$

where  $\gamma$  is the Lorentz factor of the scattering particle,  $\epsilon_B \equiv B/B_q$ ,  $\rho$  is the local field line radius of curvature,  $T$  is the neutron-star temperature in units of  $mc^2$ ,  $\Delta\mu$  is the range of  $\cos\theta$  from which thermal photons arise, and  $\lambda_C$  is the reduced Compton wavelength,  $\lambda_C = 3.86 \times 10^{-11}$  cm. Near the surface of the star,  $\Delta\mu = 1$ , while at altitudes large compared to the size of the emitting region  $\Delta\mu$  decreases as an inverse-square law. The transition between the Thomson and the Klein-Nishina regimes of NRICS is at  $2\gamma T \Delta\mu = 1$  or  $\gamma = 3.2 \times 10^3 \Delta\mu^{-1} T_6^{-1}$ . Above that  $\gamma$ , NRICS is in the KN limit.

The powers emitted by these mechanisms are

$$P_N^{Th} \approx 30.7 \gamma^2 T_6^4 \Delta\mu^3 mc^2 s^{-1}, \quad 2\gamma T \Delta\mu < 1 \quad (9)$$

$$P_N^{KN} \approx 3.08 \times 10^8 T_6^2 \Delta\mu (\ln(2\gamma T \Delta\mu) + 1) mc^2 s^{-1}, \quad 2\gamma T \Delta\mu > 1 \quad (10)$$

$$P_R \approx 4.92 \times 10^{11} \gamma^{-1} B_{12}^2 T_6 \ln(\gamma T \Delta\mu \epsilon_B^{-1}) mc^2 s^{-1}, \quad \gamma T \Delta\mu \epsilon_B^{-1} > 1 \quad (11)$$

$$P_C \approx 5.63 \times 10^{-19} \gamma^4 \rho_8^{-2} mc^2 s^{-1} \quad (12)$$

where equations (9) and (10) are from Blumenthal & Gould (1970), equation (11) is from Dermer (1990), and equation (12) is the standard form for curvature radiation, c.f. Jackson (1975).

Since, for our purposes, only the gross magnitudes of these power losses are important, we treat the logarithmic terms in equations (11) and (10) as constant for the rest of the analysis. Resonant ICS peaks at low energies, so we set  $\ln(\gamma T \Delta\mu \epsilon_B^{-1}) = 1$ . Non-resonant ICS remains important even to high energies, so we set  $\ln(2\gamma T \Delta\mu) = 4$ , a value representative of the final Lorentz factor of the primary beam in pulsars where NRICS sets the PFF.

For particles moving at moderate Lorentz factors ( $\gamma < 4.6 \times 10^6 T_6^{1/2} P^{1/4}$ ), resonant and nonresonant inverse Compton scattering are the dominant energy-loss mechanisms (Sturmer 1995), while curvature dominates at higher Lorentz factors. For the rest of this section, we adopt a model in which the entire surface of the star is hot, giving  $\Delta\mu \approx 1$  for the active low-altitude region. Only NRICS is

strongly dependent on  $\Delta\mu$ , and the effects of a hot polar cap on that process are discussed in Section 5.1.1.

At moderate  $\gamma$ , NRICS generally overwhelms RICS. The Klein-Nishina NRICS process clearly produces photons with the largest possible energy, namely the entire energy of the scattering particle. If RICS is to be significant, thermal photons must be scattered into resonance with the field, so  $\gamma T > \epsilon_B$ , therefore we also have  $\epsilon_N^{Th} > \epsilon_R$ . In both Klein-Nishina and Thomson regimes, then, the NRICS photons have a higher energy than the RICS photons, and will thus pair produce after propagating a shorter distance. If the emission rates of the two processes were equal, the higher-energy NRICS photons would set the location of the PFF, simply due to their faster conversion into pairs.

At low  $\gamma$ , the RICS emission rate is greater than NRICS, but the RICS rate fades quickly at higher  $\gamma$ . RICS photons first pair produce when  $\epsilon_R > \epsilon_a$ , or at a minimum Lorentz factor of

$$\gamma_R^{min} = \frac{1}{2} \frac{\epsilon_a}{\epsilon_B} \approx 4.8 \times 10^4 B_{12}^{-2} P^{1/2}. \quad (13)$$

If NRICS produces more photons even at this minimum Lorentz factor, it will clearly dominate RICS at all later  $\gamma$ s. At  $\gamma_R^{min}$ , NRICS operates in the Thomson regime if  $2\gamma_R^{min} T < 1$ , or  $B_{12} > 4.02 T_6^{1/2} P^{1/4}$ , and in the Klein-Nishina regime otherwise. Most pulsars, then, are in the Klein-Nishina regime by the time RICS can generate pairs.

Dividing the emitting powers by the respective characteristic energies gives an estimate for the photon production rates for Klein-Nishina NRICS and RICS,

$$\dot{N}_N^{KN} \approx 1.54 \times 10^9 \gamma^{-1} T_6^2 \Delta\mu s^{-1} \quad (14)$$

$$\dot{N}_R \approx 1.08 \times 10^{13} \gamma^{-2} B_{12} T_6 s^{-1} \quad (15)$$

Given these rates, NRICS in the Klein-Nishina regime will produce more convertible photons than RICS ( $\dot{N}_N^{KN} > \dot{N}_R$ ) whenever  $\gamma > 7.0 \times 10^3 B_{12} T_6^{-1} \Delta\mu^{-1}$ . Clearly, the RICS emission is strongest at lower  $\gamma$ . However, even if we evaluate the emission rates at  $\gamma_R^{min}$ , NRICS produces more photons whenever

$$B_{12}^{KN} < 1.9 P^{1/6} T_6^{1/3} \Delta\mu^{1/3} \quad (16)$$

For pulsars with magnetic fields less than  $B_{12}^{KN}$ , RICS has no chance of determining the pair formation front; at all beam  $\gamma$ 's high enough for RICS to generate pairs, NRICS has a higher emission rate.

For fields greater than  $B_{12}^{KN}$ , the dominant process is still unclear. RICS will only dominate the creation of pair-producing photons for a small range of  $\gamma$ , and those photons will still take longer to pair-produce than the NRICS photons. As the primary beam accelerates through this range, RICS will only dominate for a short distance. If RICS produces enough pairs in that distance, then it will set the PFF, but this is likely true only for high-field pulsars. This expectation is borne out by the more detailed calculations in Section 5.

Curvature emission, on the other hand, produces photons with energy large enough to pair produce only when  $\gamma$  is on the order of  $10^7$  or higher. At this beam energy, both NRICS and RICS emission rates are negligible; the question becomes whether the beam has a chance to accelerate to such high Lorentz factors in the presence of radiative losses. In Section 5, we find that curvature radiation is only important for the short-period pulsars, due to their higher voltage.

## 4. ACCELERATION MODEL

In this paper, we adopt a simple model of the accelerating potential, based on the general relativistic frame dragging first proposed by Muslimov & Tsygan (1992), and similar to low-altitude limits of the potential derived by Muslimov & Harding (1997). In this model, the charge difference arises because, close to the star, frame dragging reduces the effective rotation frequency  $\Omega_{eff}$  to less than the observed value. The density of the beam extracted from the star equals the Goldreich-Julian charge density at the surface, but is insufficient to cancel the charge at higher altitudes as frame-dragging weakens and the effective rotation frequency approaches the asymptotic flat-space value. To maintain simplicity, we neglect any additional effects of GR, such as those of Gonthier & Harding (1994); these effects introduce no more than 10% corrections to our results.

The effective rotation rate is  $\Omega_{eff} = (1 - \kappa_g x^{-3})\Omega$ , where  $x \equiv r/R_*$  is the dimensionless distance from the center of the star and  $\kappa_g \equiv 2GI/c^2 R_*^3 \approx 0.15 I_{45} R_6^{-3}$ , with  $I$  the moment of inertia of the star. The effective Goldreich-Julian density is then  $\eta_{GJ}(x) = \eta_{GJ}^0(1 - \kappa_g x^{-3})$ , where  $\eta_{GJ}^0$  is the charge density with frame dragging neglected,  $\eta_{GJ}^0 = -\mathbf{\Omega} \cdot \mathbf{B}/2\pi c$ .

For a more detailed form of the accelerating potential, see Muslimov & Harding (1997). For our purposes, we divide the potential into two portions: the low-altitude quadratic potential at the surface of the star, representing the fringe fields, and a high-altitude linear potential. The linear form of the high-altitude potential assumes that the distance above the star,  $s \equiv x - 1$ , is less than 1;  $s < 1/2$  suffices. The low-altitude fringe fields occupy  $s < \theta_c \ll 1$ . We assume the cross section of the polar flux tube to be round with cross sectional area  $\pi\theta_c^2 R_*^2 x^3$ , as is consistent with observations of pulsar beaming morphology (Lyne & Manchester 1988; Kramer, et al. 1998).

Due to the conducting boundary of the surface of the polar cone, the high-altitude form of the field is simply that of a slightly flared cylindrical charged waveguide operated below cutoff. Assuming that the beam density matches the Goldreich-Julian density at the stellar surface, the difference in charge density at high altitudes is  $\Delta\eta(s) = -3\kappa_g \eta_*^0 (B(x)/B_*)s$ , where  $\eta_*^0 \equiv \eta_{GJ}^0(R_*)$ . Since this is above the fringe field zone, the induced electric field is almost cylindrically radial, giving a potential of  $\Phi = \pi\theta_c^2 R_*^2 (1 - w^2) (B_* \Delta\eta(s)/B(x))$ , where  $\theta_c$  is the colatitude of the last closed field line,  $\theta_c = \sqrt{\Omega R_*/c}$ ,  $w$  is the fractional position across the polar cap,  $w \equiv \theta_*/\theta_c$ , and  $\theta_*$  is the colatitude of the footprint on the stellar surface of the current field line.

Using the potential drop across the polar cap,  $\Phi_{cap} = \theta_c^2 \Phi_0$ , where  $\Phi_0 \equiv 4\pi\eta_*^0 R_*^2$  is a pole-to-equator estimate of the potential, the potential of a field line at high altitudes becomes

$$\Phi_{high}(s) = \frac{3}{4}\kappa_g \Phi_{cap} s(1 - w^2). \quad (17)$$

Numerically,  $\Phi_0 = 1.26 \times 10^{17} B_{12} P^{-1} V$  and  $\Phi_{cap} = 2.63 \times 10^{13} B_{12} P^{-2} V$  where we have neglected the  $\cos\alpha$  inclination term as it is of order 1. This produces an order of magnitude stronger acceleration for  $P \sim 1$  sec than the previous models of Arons & Scharlemann (1979), which depended on the curvature of the field lines to generate

the starvation electric field. For  $P \lesssim 10$  ms, however, the frame dragging and field curvature acceleration mechanisms are comparable.

The low-altitude field can be treated as that of a plane-parallel charged slab, so we expect the potential to increase quadratically. The low-level charge density is slightly different from the Goldreich-Julian density. Following the method of Arons & Scharlemann (1979), we choose this density difference and the height of the transition between the low and high so that the potential and electric field are continuous.

This gives a low-altitude potential of

$$\Phi_{low} = \frac{1}{2}\Phi_0 \kappa_g s^2 (\sqrt{6}\theta_c(1 - w^2)^{1/2} - s) \quad (18)$$

where the transition between the low and high forms of the potential occurs at  $s = \sqrt{3/2}\theta_c(1 - w^2)^{1/2}$ .

To reduce this to an even more convenient form, we drop the cubic term from the low-altitude potential and simply extend the quadratic component until it meets the high-altitude linear potential. This occurs at

$$s_1 \equiv \frac{1}{2}\sqrt{\frac{3}{2}}\theta_c(1 - w^2)^{1/2} = 8.87 \times 10^{-3} P^{-1/2} (1 - w^2)^{1/2}. \quad (19)$$

If we express the particle Lorentz factor in terms of the scaled height,  $t \equiv s/s_1$ , we obtain

$$\begin{aligned} \gamma_{low}(t) &= \gamma_1 t^2, & t < 1 \\ \gamma_{high}(t) &= \gamma_1 t, & t > 1 \end{aligned} \quad (20)$$

where

$$\gamma_1 \equiv \frac{3}{8}\sqrt{\frac{3}{2}}\kappa_g \theta_c^3 \frac{e\Phi_0}{mc^2} = 5.14 \times 10^4 B_{12} P^{-5/2} (1 - w^2)^{3/2}. \quad (21)$$

Although we have dropped the smooth transition in electric field from low to high as an approximation, we are still using that underlying model to set the coefficient. The approximation is valid as long as the acceleration is not radiation reaction limited for particle energies  $\approx \gamma_1$ , so that  $\gamma \propto \Phi$ , as is true of all of our models.

This acceleration is strong enough that we can ignore the effects of radiative losses on the beam particles due to ICS, so this discontinuous electric field causes no difficulties. Since the power produced by ICS declines with increasing Lorentz factor, once the beam has accelerated a short distance above the stellar surface, the ICS losses become negligible. Curvature radiation becomes very efficient at high Lorentz factor, so if the beam reaches a Lorentz factor of order a few times  $10^7$ , curvature radiation will hold it there. We will return to this issue when we discuss curvature radiation in more depth.

For the remainder of the paper, we simply drop the dependence on  $w$  from the potential, in effect examining the activity on a typical field line, where neither  $w$  nor  $1 - w$  is small.

## 5. PAIR FORMATION FRONT

The primary beam from the star will accelerate due to the starvation electric field until the beam has produced a pair plasma dense enough to short out the field. Several authors have located this pair formation front (PFF) at the point where photons emitted by the primary beam first reach an optical depth of one, with regards to the

pair-creation opacity. This heuristic was first suggested by Ruderman & Sutherland (1975) for curvature-dominated cascades, and in that case, it is valid. For curvature radiation, further acceleration of particles only increases both the energy and number of emitted photons, resulting in a sharp front of pair production.

However, if inverse Compton radiation is the primary source of convertible photons, this approximation breaks down. As the primary beam accelerates, the energy of the ICS photons increases, but their number drops. Rather than the copious cascades produced by curvature radiation, where the PFF is a sharp transition, ICS tends to produce more gradual cascades where a small number of high-energy particles set off a lengthy cascade of pair production. For inverse Compton processes, then, it is not guaranteed that the potential will be shorted out as soon as the first pair is produced.

To properly calculate the location of the pair formation front in the face of relatively sparse photon production, we have to track not only the height at which photons of a certain energy are emitted and the distance those photons travel before pair producing, but also the number of such photons produced and the number of secondary pairs produced by the resulting synchrotron cascade. In short, we have to integrate the pair production rate until we reach some threshold. Since inertial frame dragging induces a fractional difference of the beam density from the Goldreich-Julian density of approximately  $\kappa_g$ , we set the location of the pair formation front by equating the number of pairs created per primary particle to  $\kappa_g$ .

### 5.1. PFF Position

As discussed in Section 3, for each emission mechanism we approximate the emitted number spectrum by assuming that all of the power goes into creating photons at the respective characteristic maximum energy:

$$\dot{N}_X(\epsilon) \approx \frac{P_X(\gamma)}{\epsilon_X(\gamma)} \delta(\epsilon - \epsilon_X(\gamma)) \quad (22)$$

where  $X \in \{C, NR, R\}$ , and  $P_X(\gamma)$  and  $\epsilon_X(\gamma)$  are again the total power and the maximum energy emitted by particles with Lorentz factor  $\gamma$  due to curvature (C), nonresonant ICS (NR), or resonant ICS (R) emission.

Using the cascade multiplicity (4), the total number of pairs produced by one primary particle before a height  $s$  may be divided into a portion due to the primary photons themselves,  $N_{\pm 1}$ , and a portion due to the subsequent cascade of secondaries,  $N_{\pm 2}$ , where

$$N_{\pm}(s) = N_{\pm 1}(s) + N_{\pm 2}(s) \quad (23)$$

$$N_{\pm 1}(s) = \int_{s_{min}}^{s_{max}} ds' R_* \frac{P_X(s')}{c\epsilon_X(s')} \quad (24)$$

$$N_{\pm 2}(s) = \frac{4}{\sqrt{\ln \Lambda}} \int_{s_{min}}^{s_{max}} ds' R_* \frac{P_X(s')}{c\epsilon_a} (s - s') \quad (25)$$

where  $s_{min}$  and  $s_{max}$  are the first and last heights at which the primary beam emits photons capable of pair producing at or below  $s$ . We neglect the variation of  $\epsilon_a$  with  $s'$ , making an on-the-spot approximation.

These heights are the values of  $s_e$  which satisfy

$$\Delta s(\epsilon_X(s_e)) = s - s_e \quad (26)$$

with  $\Delta s$  from equation (2). For fast acceleration,  $s_{min} \ll s$  and  $s - s_{max} \ll s$ , so these limits are approximately given by

$$\epsilon_X(s_{min}) \approx \frac{\epsilon_a}{4s} \quad (27)$$

$$s_{max} \approx s - \frac{1}{4} \frac{\epsilon_a}{\epsilon_X(s)} \quad (28)$$

The lower height  $s_{min}$  is the distance required to accelerate particles to energies capable of pair producing in a distance  $s$ , while  $s_{max}$  is  $s$  reduced by the distance it would take a photon emitted at  $s$  to pair produce. By the time a pulsar beam has reached an altitude where the PFF forms, it has typically reached a high energy, so  $s_{max} \approx s$ . The form of  $s_{min}$ , however, will depend on the regime of the potential in which it falls. Since the potential switches from its low-altitude form to its high-altitude form at  $s = s_1$ , it is easiest to calculate in terms of the scaled distance,  $t \equiv s/s_1$ .

#### 5.1.1. Non-resonant ICS

As the beam pulled from the stellar surface accelerates to high  $\gamma$ , it will pass from the Thomson regime of NRICS into the Klein-Nishina regime. Since this acceleration is extremely strong, this transition will occur close to the stellar surface, and we can simply use the Klein-Nishina form of NRICS for these calculations. For NRICS in the KN regime,  $P_{NR}(\gamma)$  is only logarithmically dependent on  $\gamma$ , so we treat it as effectively constant. Since the power is then independent of the Lorentz factor, the NRICS cascade is insensitive to the details of the accelerating potential.

Furthermore, since the NRICS process generates comparatively few photons, it can only achieve high pair multiplicities through extended cascades of secondaries. Using the NRICS power, equation (10), in the secondary portion of the multiplicity, equation (23), produces a total multiplicity as a function of height of

$$N_{\pm NR}(t) = 2 \frac{P_{NR}}{\epsilon_a \sqrt{\ln \Lambda}} \frac{s_1^2 R_*}{c} (t - t_{min})^2 \quad (29)$$

The critical energy is  $\epsilon_{NR} = \gamma$ , so if we define  $t'_{min} \equiv \epsilon_a/4s_1\gamma_1 t$ , then  $t_{min} = t'_{min}/2$  if  $t'_{min} < 1$  and  $t_{min} = t'_{min}$  otherwise.

Typically, however, the PFF only forms at  $t \gg t_{min}$ , so we can neglect  $t_{min}$  above. The distance to achieve a pair multiplicity of  $\kappa$  is then

$$t = \left( \frac{\kappa \epsilon_a \sqrt{\ln \Lambda}}{2P_{NR}} \frac{c}{s_1^2 R_*} \right)^{1/2} \quad (30)$$

The PFF takes place where  $\kappa = \kappa_g$ , or

$$t_{PFF, NR} = 13.4 B_{12}^{-1/2} P^{3/4} T_6^{-1} f_\rho^{1/2} \quad (31)$$

assuming, as before,  $\kappa_g = 0.15$ . In terms of the stellar radius, this is

$$s_{PFF, NR} = 0.119 B_{12}^{-1/2} P^{1/4} T_6^{-1} f_\rho^{1/2} \quad (32)$$

For most pulsars, this is well above the regime of the fringe fields,  $t \approx 1$ . Likewise, it is still within the linear region of the potential ( $s < 1$ ), provided that  $B > 2 \times 10^{10}$  G. Very young and energetic pulsars may have  $t_{PFF} < 1$ , as discussed in Section 6. The above formalism remains valid regardless.

If only the polar cap is hot, the flux of thermal X-rays is roughly halved by  $t = 1$ , reducing the number of pairs produced. If we model a hot polar cap by applying the same technique as above, but attenuating the ICS source at  $t > 1$  by  $1/t^2$ , we find that the pair formation front occurs at

$$t_{\text{PFF,NR}}^{\text{cap}} = 45.0 B_{12}^{-1} P^{3/2} T_6^{-2} f_\rho \quad (33)$$

or

$$s_{\text{PFF,NR}}^{\text{cap}} = 0.399 B_{12}^{-1} P T_6^{-2} f_\rho \quad (34)$$

As expected, the PFF occurs at higher altitudes if only the polar cap is hot.

### 5.1.2. Resonant ICS

In general, resonant inverse Compton scattering depends on the large resonant cross section to compete with nonresonant scattering. The RICS photons are typically lower energy than the NRICS photons and produce less of a cascade. As such, the pair production of the primaries dominates that of the secondaries, and we use equation (24) to compute the multiplicity.

The steps of computing the PFF height are the same as for NRICS, using the primary-only integral (24) rather than equation (25) and  $t'_{\text{min}} = \epsilon_a / 8\epsilon_B s_1 \gamma_1 t$ .

Since the emission rate depends on particle  $\gamma$ , the two forms of the accelerating potential yield different results. There are three major regimes: where the pair formation front forms in the low-altitude region, with  $t, t_{\text{min}} < 1$ , where the PFF forms in the upper region due to photons emitted in the lower, with  $t_{\text{min}} < 1$  but  $t > 1$ , and where the entire process takes place in the high-altitude potential, with  $t, t_{\text{min}} > 1$ .

In practice, RICS is only important when it can create pairs in the low-altitude potential with  $t_{\text{min}} < 1$ . If that is so, the number of pairs produced as a function of distance in both cases is, to leading order in  $t_{\text{min}}$ ,

$$N_{\pm R}(t) = \frac{1}{3} \frac{P_R(\gamma_1)}{2\gamma_1 \epsilon_B} \frac{s_1 R_*}{c} t_{\text{min}}^{-3} \quad (35)$$

which gives a PFF height of

$$t_{\text{PFF,R}} = 1350 B_{12}^{-7/3} P^{1/2} T_6^{-2/3} f_\rho. \quad (36)$$

or

$$s_{\text{PFF,R}} = 12.0 B_{12}^{-7/3} T_6^{-2/3} f_\rho. \quad (37)$$

### 5.1.3. Curvature Radiation

Curvature radiation differs from both ICS processes in that, as the beam Lorentz factor increases, both the emission rate and the average photon energy increase. This increase creates a sharp transition in the pair production rate once the particle  $\gamma$  reaches the minimum required to pair-produce. Due to this quick generation of a copious pair plasma, both the  $N_{\pm 1}$  (24) and  $N_{\pm 2}$  (25) forms of the multiplicity lead to nigh-identical results for the PFF height. In practice, we find that the approximation derived from  $N_{\pm 2}$  better fits the numerical solution, so we will concentrate on that case.

The curvature power (12) and critical energy (8) give for  $t, t_{\text{min}} < 1$ ,

$$N_{\pm C}^{\text{low}} = \frac{2}{45} \frac{P_C(\gamma_1)}{\epsilon_a \sqrt{\ln \Lambda}} \frac{s_1^2 R_*}{c} (t^{10} - 10 t t_{\text{min}}^9 + 9 t_{\text{min}}^{10}) \quad (38)$$

and for  $t, t_{\text{min}} > 1$ ,

$$N_{\pm C}^{\text{high}} = \frac{2}{15} \frac{P_C(\gamma_1)}{\epsilon_a \sqrt{\ln \Lambda}} \frac{s_1^2 R_*}{c} (t^6 - 6 t t_{\text{min}}^5 + 5 t_{\text{min}}^6) \quad (39)$$

The mixed case is unimportant, due to the strong  $t$ -dependence of the multiplicity.

As before,  $t_{\text{min}}$  is the first point at which the beam has reached a sufficient Lorentz factor for the curvature photons to pair-produce by  $t$ ,

$$t_{\text{min}} \approx \left( \frac{\epsilon_a \rho}{6 \lambda_C s_1 t} \right)^{1/3} = 894 t^{-1/3} B_{12}^{-4/3} P^3 f_\rho^{2/3} \quad (40)$$

Since the power produced by curvature radiation increases strongly with increasing  $\gamma$ , the pair multiplicity is dominated by the emission from the upper end of the range, so we can obtain a simple approximation by assuming  $t_{\text{min}} = 0$ . As most pulsars are in the  $t_{\text{PFF}} > 1$  regime, except for the shortest-period millisecond pulsars, we concentrate on high- $t$ , giving

$$t_{\text{PFF,C}}^{\text{high}} \approx 98.2 B_{12}^{-5/6} P^{25/12} f_\rho^{1/2} \quad \text{if } t_{\text{PFF,C}}^{\text{low}} > 1 \quad (41)$$

When compared to the result of numerically solving for  $t$ , this is only correct to within a factor of 2–3. This discrepancy arises because once curvature emission is active, it very rapidly shorts out the field, so  $t_{\text{PFF}}$  is close to  $t_{\text{min}}$ . Neglecting  $t_{\text{min}}$ , while giving a straightforward expression for the PFF height, introduces an appreciable error. The results given in subsequent sections use the full numerical solution to the polynomials (38) and (39) for  $t_{\text{PFF,C}}$ ; equation (41) should be considered a rough estimate.

In terms of stellar radius, the high-altitude limit becomes

$$s_{\text{PFF,C}}^{\text{high}} \approx 0.678 B_{12}^{-5/6} P^{19/12} f_\rho^{1/2}. \quad (42)$$

This depends primarily on the polar cap potential, as  $s_{\text{PFF}} \propto \Phi_{\text{cap}}^{-5/6} P^{-1/12}$ . Physically, obtaining any pair production from curvature emission requires high potentials and beam Lorentz factors.

These results are inaccurate, however, for the millisecond pulsars, because radiation reaction prevents the primary beam from accelerating to the high Lorentz factors needed to generate photons capable of pair-producing in the low magnetic fields. The high-altitude accelerating electric field is

$$E = \frac{\gamma_1}{s_1} \frac{m c^2}{e R_*}. \quad (43)$$

The acceleration due to this field is balanced by the curvature power loss at a Lorentz factor of

$$\gamma_{\text{bal}} = 2.26 \times 10^7 B_{12}^{1/4} P^{-1/4} f_\rho^{1/2}. \quad (44)$$

Setting the typical curvature photon energy at  $\gamma_{\text{bal}}$  to  $\epsilon_a$ ,  $\epsilon_C(\gamma_{\text{bal}}) = \epsilon_a$ , and solving for the magnetic field yields

$$B_{12} = 0.500 P f_\rho^{2/7} \quad (45)$$

At fields lower than this, radiation reaction will prevent curvature radiation from creating pairs. We cannot yet conclude that at higher fields, curvature photons will create pairs, merely that radiation reaction will not prevent it.

If the magnetic field has a radius of curvature of  $\rho = R_*$ , or  $f_\rho = 0.011 P^{-1/2}$ , then the limiting magnetic field becomes

$$B_{12} = 0.137 P^{6/7}, \quad (46)$$

which would allow more pulsars to pair-produce via curvature radiation.

### 5.2. Beam Lorentz Factor

The PFF is located at

$$t_{PFF} = \min(t_{PFF,NR}, t_{PFF,R}, t_{PFF,C}). \quad (47)$$

Since the beam stops accelerating at this point, its final Lorentz factor is

$$\gamma_{beam} = \gamma_1 t_{PFF}^2, \text{ if } t_{PFF} < 1 \quad (48)$$

$$\gamma_{beam} = \gamma_1 t_{PFF}, \text{ if } t_{PFF} > 1 \quad (49)$$

Analytically, the estimated final Lorentz factors for each emission process, assuming  $t_{PFF} > 1$ , are

$$\gamma_{NR} = 6.90 \times 10^6 B_{12}^{1/2} P^{-7/4} T_6^{-1} f_\rho^{1/2} \quad (50)$$

$$\gamma_R = 6.95 \times 10^7 B_{12}^{-4/3} P^{-2} T_6^{-2/3} f_\rho \quad (51)$$

$$\gamma_C = 5.05 \times 10^6 B_{12}^{1/6} P^{-5/12} f_\rho^{1/2}. \quad (52)$$

Since the smallest  $t_{PFF}$  sets the gap height, the dominant mechanism is the one with the lowest predicted beam  $\gamma$ .

### 5.3. Polar Cap Heating

Basic electrodynamics requires that a fraction of the positrons created above the PFF be reversed and accelerated back down onto the surface of the star, heating it. In the curvature-starvation acceleration model of Arons & Scharlemann (1979), this flux is  $\theta_c^2 n_{GJC}$ , while in the frame-dragging-starvation model, we expect a reversed flux on the order of  $\kappa_g \theta_c n_{GJC}$ , where  $n_{GJ} \equiv \eta_{GJ}/e$  is the fiducial Goldreich-Julian number density, see Harding & Muslimov (1998); Zhang & Harding (2000); Zhang, et al. (2000).

Since these reversed particles are accelerated through the same potential as the primary beam, they strike the polar cap with a Lorentz factor  $\gamma_{PFF}$ . The downward energy flux is then

$$\phi = \gamma_{PFF} m c^2 f_{rev} n_{GJC} \quad (53)$$

where  $f_{rev}$  is the fraction of the Goldreich-Julian flux that is reversed. The energy is then radiated away by a surface black body, yielding a polar cap temperature

$$T_{cap} = \left( \frac{\gamma_{PFF} m c^2 f_{rev} n_{GJC}}{\sigma_{SB}} \right)^{1/4} \quad (54)$$

$$= 3.9 \times 10^6 B_{12}^{1/2} P^{-3/4} \left( f_{rev} \frac{\gamma_{PFF} m c^2}{e \Phi_{cap}} \right)^{1/4} K \quad (55)$$

Since the value of  $\gamma_{PFF}$  for the ICS processes itself depends on the stellar temperature, we can solve equation (54) for the self-consistent cap temperature and, from that, derive the PFF height due to each process. Setting  $f_{rev} = \kappa_g \theta_c$ , this yields cap temperatures of

$$T_{6,NR} = 0.730 B_{12}^{1/6} P^{-5/12} f_\rho^{1/6} \quad (56)$$

$$T_{6,R} = 1.38 B_{12}^{-1/14} P^{-3/4} f_\rho^{3/14} \quad (57)$$

$$T_{6,C} = 0.758 B_{12}^{7/24} P^{-23/48} f_\rho^{1/8} \quad (58)$$

where we have assumed that  $t_{PFF} > 1$ , using equation (36) for RICS, the attenuated NRICS expression, equation (33), and equation (49) for the resultant Lorentz factor. If  $t_{PFF} < 1$ , the appropriate corresponding equations would be (36), (31), and (48). For curvature, only the

high-altitude form is important, equation (41). The low-altitude expressions yield

$$T_{6,NR}^{low} = 0.919 B_{12}^{1/6} P^{-5/12} f_\rho^{1/6} \quad (59)$$

$$T_{6,R}^{low} = 5.13 B_{12}^{-1/2} P^{-9/16} f_\rho^{3/8}. \quad (60)$$

The low-altitude forms are most appropriate for the youngest, highest potential pulsars.

These temperatures correspond to PFF heights of

$$s_{PFF,NR,pc} = 0.749 B_{12}^{-4/3} P^{11/6} f_\rho^{2/3} \quad (61)$$

$$s_{PFF,R,pc} = 9.66 B_{12}^{-16/7} P^{1/2} f_\rho^{6/7} \quad (62)$$

$$s_{PFF,NR,pc}^{low} = 0.129 B_{12}^{-2/3} P^{2/3} f_\rho^{1/3} \quad (63)$$

$$s_{PFF,R,pc}^{low} = 4.92 B_{12}^{-2} P^{3/8} f_\rho^{3/4} \quad (64)$$

Since the curvature PFF height does not depend on the temperature, it remains as given in equation (42).

The regimes in which these expressions apply are somewhat complex. The predicted PFF height depends on whether the pulsar is in the  $t < 1$  or  $t > 1$  regime. For each of RICS and NRICS, if  $t_{PFF}^{low} \equiv s_{PFF}^{low}/s_1 < 1$ , then the low-altitude variant is appropriate, otherwise the high-altitude. The shortest PFF height then determines the dominant mechanism and the temperature of the polar cap.

However, if the stellar temperature, as derived from a cooling model, is higher than this predicted temperature, then the polar heating is irrelevant and the normal whole-star PFF heights apply instead, equations (32) and (37).

### 5.4. Final Pair Multiplicity

Although the beam acceleration stops at  $t_{PFF}$ , the primary particles will continue to produce pairs even after the PFF. After the PFF, cascades fall into two general categories: opacity-bounded and energy-bounded. Opacity-bounded cascades are primarily limited by the decline of the magnetic field with distance from the star; to first order, the beam Lorentz factor remains constant. Energy-bounded cascades, by comparison, are limited by the amount of energy in the beam capable of being converted into pairs. Here the beam loses energy faster than the magnetic field drops.

Most pulsars dominated by inverse Compton processes are opacity bounded. By the time the beam has reached the PFF, it has typically accelerated to a Lorentz factor large enough that further Compton losses are negligible. Pulsars dominated by curvature emission, however, are energy-bounded. Once the beam has a Lorentz factor high enough to make pairs via curvature radiation, radiative losses quickly slow the beam once the accelerating potential has been shorted out.

For NRICS from a hot star, the final number of pairs generated may then be approximated by counting the number of pairs produced by a constant- $\gamma$  beam,

$$\kappa_{NR} = \frac{1}{\sqrt{\ln \Lambda}} \int_0^\infty ds \frac{R_* P_{NR}}{c \epsilon_a(s)}. \quad (65)$$

Since  $\epsilon_a(s) = \epsilon_a^0 (1+s)^{-7/2}$ , this becomes

$$\kappa_{NR} = \frac{2}{5} \frac{P_{NR} R_*}{\epsilon_a^0 \sqrt{\ln \Lambda} c} = 2.1 B_{12} P^{-1/2} T_6^2 f_\rho^{-1}. \quad (66)$$

If only the polar cap is hot, this is reduced by dilution to

$$\kappa_{NR}^{cap} = 2 \frac{P_{NR} s_1 R_*}{\epsilon_a^0 \sqrt{\ln \Lambda} c} = 0.094 B_{12} P^{-1} T_6^2 f_\rho^{-1}, \quad (67)$$

using the same approximate attenuation model ( $\propto t^{-2}$  for  $t > 1$ ).

For RICS, the total number of pairs generated is dominated by photons which are emitted below the PFF, but which are absorbed above it. The minimum height for pair production is  $t_R^{min} = (\epsilon_a/2\gamma_1\epsilon_B)^\alpha$ , where, as before,  $\alpha = 1$  for  $t_R^{min} > 1$  and  $\alpha = 1/2$  otherwise.

The number of pairs produced by the primary photons is comparable to that produced by the cascade, so the multiplicity is

$$\kappa_R = \int_{t_R^{min}}^{t_R^{min}} dt \frac{s_1 R_*}{c} \frac{P_R(\gamma(t))}{2\gamma(t)\epsilon_B} \left( 1 + \frac{1}{\sqrt{\ln \Lambda}} \frac{2\gamma(t)\epsilon_B}{\epsilon_a} \right). \quad (68)$$

If  $t_R^{min} < 1$ , the total pair production is dominated by the region below  $t = 1$ , so  $t_R^{max} = 1$ ; otherwise, the pair production is truncated by the decline of the magnetic field on the scale of  $R_*$  and  $t_R^{max} \approx s_1^{-1}$ .

This gives two expressions for the final multiplicity, the low-altitude estimate, appropriate when  $B_{12} \gtrsim P$ ,

$$\kappa_R^{low} = 7.5 \times 10^{-4} B_{12}^{7/2} T_6 f_\rho^{-3/2} \quad (69)$$

and the high-altitude estimate, appropriate when  $B_{12} \lesssim P$ ,

$$\kappa_R^{high} = 0.0013 B_{12}^2 P^{3/2} T_6 f_\rho^{-1} \left( 1 + \frac{4.8 + 3 \ln B_{12} - 2.5 \ln P}{\sqrt{\ln \Lambda}} \right) \quad (70)$$

If curvature sets the PFF, the cascade is energy-bounded, and the total number of pairs is roughly the overshoot energy of the beam, converted into pairs with energy  $\epsilon_a$ . If  $\gamma_C^{min}$  is the minimum Lorentz factor required to pair produce, the total number of pairs expected is

$$\kappa_C = \frac{\gamma_C^{PFF} - \gamma_C^{min}}{\epsilon_a \sqrt{\ln \Lambda}} \quad (71)$$

where

$$\gamma_C^{min} = \left( \frac{2}{3} \frac{\rho}{\lambda_C} \epsilon_a \right)^{1/3} = 1.51 \times 10^7 B_{12}^{-1/3} P^{1/3} f_\rho^{2/3}. \quad (72)$$

This expression for  $\kappa_C$  depends critically on the slight difference between the beam Lorentz factor and  $\gamma_C^{min}$ . As such, this form cannot be further simplified while maintaining accuracy.

### 5.5. Death Lines

Pulsar death occurs when pair-production is too weak to generate the multiplicity of  $\kappa_g$  required to short out the accelerating potential. This sets a minimum potential for each process, namely

$$\Phi_{NR}^{death} = 6.0 \times 10^{13} P^{-5/8} f_\rho^{1/2} V \quad (73)$$

$$\Phi_{R,low}^{death} = 1.1 \times 10^{14} P^{-57/32} f_\rho^{3/8} V \quad (74)$$

$$\Phi_{R,high}^{death} = 2.6 \times 10^{14} P^{-43/18} f_\rho^{11/27} V \quad (75)$$

where we have used the multiplicity equations (67), (69), and (70), along with the corresponding heated cap temperatures, equations (56) and (57). If the star itself is hotter than the heated caps, the stellar temperature predicted by the cooling model used should be substituted into the multiplicity equations, rather than the self-heating model.

The corresponding death line for curvature radiation is best computed by simply finding the minimum  $\Phi$  such

that the primary beam produces photons capable of pair-producing by  $s = 1$ , after which point the acceleration saturates. Including the decline of the magnetic field and the increase in the radius of curvature with increasing distance from the star gives a minimum potential of

$$\Phi_C^{min} = 8.95 \times 10^{13} P^{-1/4} f_\rho^{1/2} V \quad (76)$$

Radiation reaction, however, also sets a lower limit on the required field. Converting the magnetic field limit from equation (45) into potential units gives

$$\Phi_C^{death} = \max(8.95 \times 10^{13} P^{-1/4} f_\rho^{1/2}, 1.32 \times 10^{13} P^{-1} f_\rho^{2/7}) V. \quad (77)$$

The resulting death lines are shown in terms of the polar cap potential in Figure 1, for both the normal dipole field and a  $\rho = R_*$  configuration. As low-to-mid  $P$ , NRICS sets the death lines, although the dip near  $P = 0.1$  is due to the effects of curvature radiation. At high  $P$ , RICS sets the death line instead.

Many of the pulsars near  $P = 1$  are between the two death lines. This indicates that either non-dipolar components are important in these pulsars, or that the temperature of these objects is larger than what the self-heating model predicts. We consider non-dipolar effects, namely an offset dipole, to be the most likely explanation.

### 5.6. Particle Injection into the Crab Nebula

Study of the emission from the plerions surrounding pulsars can provide empirical constraints on the pair multiplicity  $\kappa$ . The best studied case is the Crab Nebula, energized by its central pulsar, which has a rotation period of 33 msec and an inferred magnetic dipole moment  $\mu = 3.6 \times 10^{30}$  cgs. For this pulsar, our results yield  $\kappa \approx 5 \times 10^4$ . The Goldreich-Julian rate of elementary charge loss is  $\dot{N}_{GJ} = 2\Omega^2\mu/ec = 1.8 \times 10^{34} \text{ s}^{-1}$ . The pulsar's geometry is such that the primary polar cap current extracted by the starvation electric field is made of electrons. Then the total rate of injection of electrons and positrons into the nebula implied by our model is  $\dot{N}_{e^+ + e^-} = 2\kappa\dot{N}_{GJ} \approx 1.8 \times 10^{39} \text{ s}^{-1}$ .

The nebular X-ray emission from the equatorial torus (Hester, et al. 1995) constrains the electron plus positron injection rate from the pulsar into the visible equatorial region to be approximately  $(1 - 2) \times 10^{37} \text{ particles s}^{-1}$  (Kennel & Coroniti 1984; Gallant & Arons 1994, J. Arons & A. Spitkovsky, in preparation). The flow feeding the equatorial region fills a latitudinal sector with full angular width of approximately  $2\delta \sim 20^\circ$ , assuming the flow from the wind termination shock to the visible torus is purely radial. If the pair outflow from the pulsar is spherically symmetric, our model of the multiplicity implies  $\sim 3 \times 10^{38}$  electrons and positrons per second are being fed into the equatorial X-ray emitting region, well more than enough to explain the X-ray observations.

In reality, both non radial divergence of the post shock flow in the nebula and the likely decline of the pair flux toward the boundaries of the polar flow (the region of the polar cap outflow which feeds the equatorial) both suggest that our estimate of the particle flux *into the X-ray torus* is an upper limit. Therefore we conclude that polar cap pair creation in the Crab pulsar is adequate to fully explain the present day particle injection rate measure by X-ray



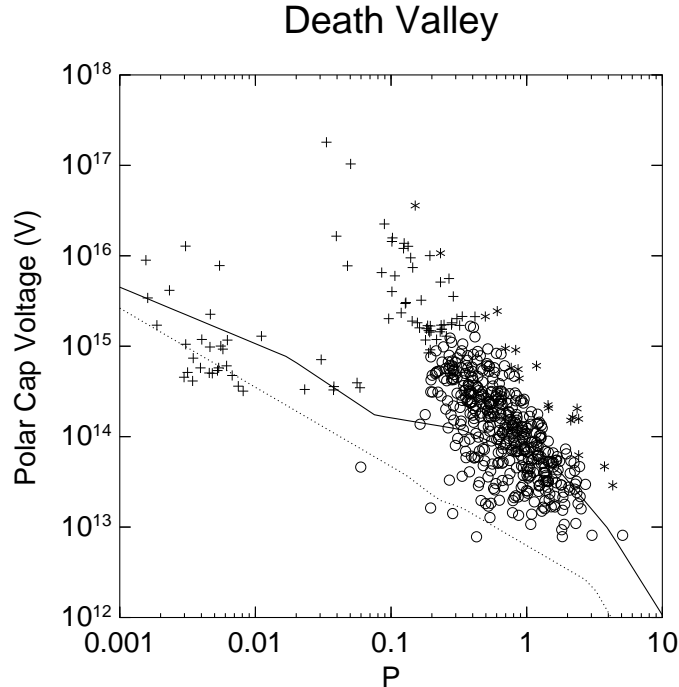


FIG. 1.— Pulsar death lines for a self-heated polar cap. The solid line is the death line for a dipole magnetic field, while the dotted line assumes a  $\rho = R_*$  multipole field. Pulsars, in the dipole case, dominated by NRICS are marked with circles, those dominated by RICS are marked with stars, and those dominated by curvature are marked with crosses.

observations of the Crab Nebula. Other plerions will be considered elsewhere.

By contrast, it is not so clear that polar cap pair creation can explain the *total* particle injection rate into the Crab. It has long been known that the radio emission from the Nebula requires a particle injection rate, *averaged over the Nebula's history*, of approximately  $10^{40}\text{s}^{-1}$  (e.g. Rees & Gunn (1974)), an estimate probably uncertain to a factor of 3. Our calculations yield a total injection rate *today* about a factor of 5 below the average rate required to explain the radio emission, assuming no Nebular evolution.

Whether this discrepancy is a serious problem is unclear. The estimate of the average rate of pair injection assumes the Nebula to be a homogeneous synchrotron source - clearly, it is not. The pair creation rate probably was higher in the past, when the pulsar was rotating somewhat more rapidly, so long as the star was cool enough for pair creation to operate on the curvature dominated branch shown in Figure 5, as is the case today. On the other hand, adiabatic losses as the nebula expands might increase the required average rate. An additional magnetospheric source of particles, such as an outer gap, may exist. These more sophisticated nebular modeling and global magnetospheric questions are outside the scope of our investigation, and we leave this subject with the remark that polar cap pair creation *may* be adequate to explain the total particle injection rate into this well known synchrotron source, but the case is not as clear as it is for understanding the injection of the particles that create the high energy synchrotron emission. The application of our models to other pulsar-plerion systems is also a topic for a separate investigation.

## 6. DISCUSSION

A broad survey, such as this, best answers broad questions about the population. With these results, we seek to answer two questions, namely “Which gamma-ray emission mechanism dominates in which region of pulsar space?” and “How well does this model explain the observed distribution of pulsars in  $P$ - $\dot{P}$  space?”

For any pulsar, the smallest of  $t_{PFF,R}$ ,  $t_{PFF,NR}$ , and  $t_{PFF,C}$  sets the height of the pair formation front. For a whole-star temperature of  $10^6$  K, assuming no special field configuration, the pulsars of the Princeton pulsar catalog (Taylor, et al. 1993) are categorized as shown in Figure 2. Figure 3 shows this same dataset in terms of the more physical variables of surface magnetic field and polar cap voltage. This categorization depends on the assumed temperature and size of the thermally emitting region, but several basic conclusions can still be drawn. The largest-field pulsars tend to be dominated by RICS, the largest-voltage by curvature radiation, and the rest by NRICS.

As can be seen in Figure 3, the important boundaries are between curvature and NRICS at high voltage and between NRICS and RICS at high magnetic field. Comparing the predicted PFF heights due to RICS and NRICS yields

$$\frac{t_{PFF,NR}}{t_{PFF,R}} = 0.0099 B_{12}^{11/6} P^{1/4} T_6^{-1/3} f_\rho^{-1/2}. \quad (78)$$

The boundary between NRICS and RICS is almost completely set by the magnetic field. RICS will dominate only for pulsars with very high fields,  $B_{12} > 12.4 P^{-3/22} T_6^{2/11}$ .

Similarly, comparing the PFF heights due to curvature and NRICS yields

$$\frac{t_{PFF,C}^{high}}{t_{PFF,NR}} = 7.3 B_{12}^{-1/3} P^{4/3} T_6, \quad (79)$$

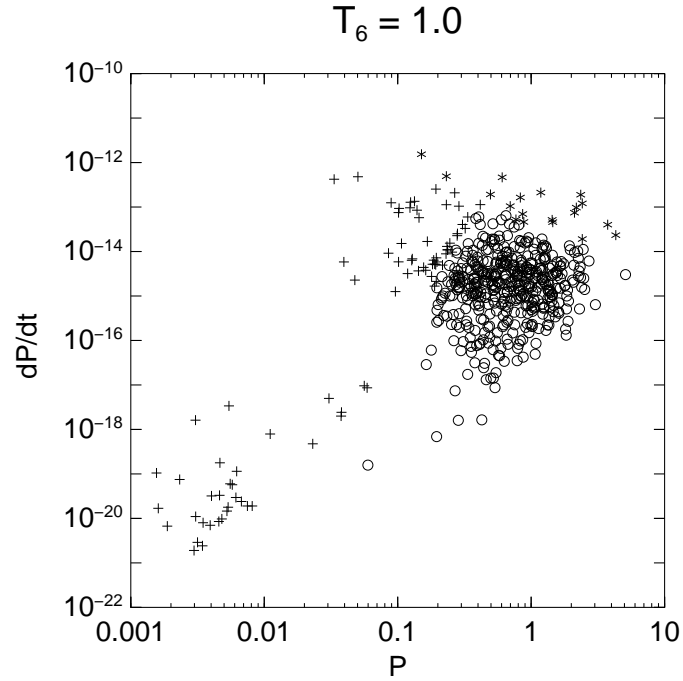


FIG. 2.—  $P - \dot{P}$  diagram showing which pulsars have the PFF height set by curvature (crosses), NRICS (circles), and RICS (stars)

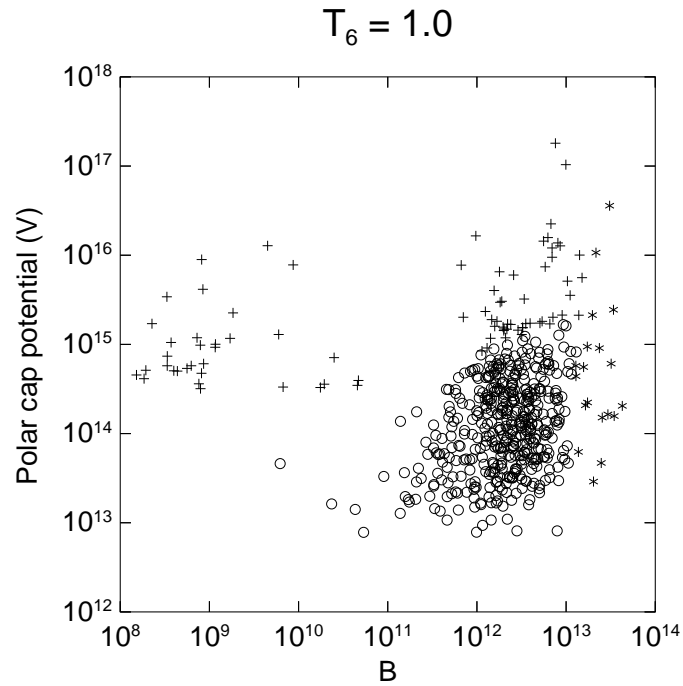


FIG. 3.—  $B - \Phi_{cap}$  diagram showing which pulsars have the PFF height set by curvature (crosses), NRICS (circles), and RICS (stars). Curvature dominates at high  $\Phi_{cap}$ , while RICS dominates high  $B$ .

Whenever this ratio is less than one, the PFF is set by curvature emission; in this regime, RICS is never important. Thus, curvature dominates whenever  $P < 0.22 B_{12}^{1/4} T_6^{-3/4}$ . This boundary is less sensitive to the magnetic field than that between RICS and NRICS, but depends more strongly on the temperature.

Perhaps the more interesting question is where this theory can comfortably generate enough pairs to short out the accelerating potential, assuming that pair creation is required for pulsar emission. Since many pulsars are dominated by NRICS, and NRICS depends strongly on the size and temperature of the thermally emitting region, both the cooling model chosen for the pulsar and the degree of polar-cap heating are extremely important.

The case of a cool ( $10^5$  K) star with the self-consistent polar cap temperatures derived in Section 5.3 is shown in Figure 4. Using the polar cap NRICS multiplicity, equation (67), we find that the cascade cannot produce sufficient pairs to short out the electric field if the predicted PFF is above  $s_{PFF} = 0.25$ . Given this criterion, this model succeeds for pulsars with timing ages less than about  $10^7$  years, but fails for older pulsars.

Figure 5 shows the results of adopting a cooling model derived from Tsuruta (1998), which includes the effects of the magnetic field on thermal conductivity, but no polar cap heating. Since heat conduction is easier along magnetic field lines than perpendicular to them, the polar regions remain hotter than the standard cooling of an unmagnetized pulsar, out to ages greater than  $10^6$  years. Full 2D calculations have only been extended to ages of several million years, but the polar regions show no sign of rapid cooling up to that point. For our model, we assume that more rapid cooling, with a power-law slope of  $-0.375$  begins at  $10^7$  years. This power law represents the effects of internal heating; with no additional heating, the field would decay exponentially beyond this point.

The precise temperature model used is

$$\begin{aligned} \log T &= 6.65 - 0.1 \log \tau, & \tau < 10^7 \text{ yr} \\ \log T &= 8.575 - 0.375 \log \tau, & \tau > 10^7 \text{ yr} \end{aligned} \quad (80)$$

where  $\tau$  is the spindown age of the star. This is a generous model, in that it predicts a hot polar cap to late ages, but it demonstrates the strong effect of the cooling model on the pair-creation process.

Using the NRICS multiplicity, equation (66), we find that the cascade cannot produce sufficient pairs to short out the electric field if the predicted PFF is above  $s_{PFF} = 0.45$ . The combination of magnetic cooling and internal heating allows pulsars to remain active out to timing ages of  $10^8$  years, without further modifications.

The notable exceptions in both of these cases are the oldest pulsars and the millisecond pulsars. The millisecond pulsars, for the most part, require particles to reach a Lorentz factor so large that their acceleration is truncated by radiation-reaction before reaching the threshold for pair-production, while the old pulsars simply do not provide enough voltage and field strength to pair-produce. These pulsars could all be explained by invoking a magnetic field more complicated than a simple star-centered dipole, however. Due to the success of the rotating vector model for pulsar polarization (Radhakrishnan & Cooke 1969), we believe an offset dipole to be more plausible than simply adding an arbitrary mixture of higher-order multi-

poles.

An offset dipole could both increase the surface field strength by moving the center of the dipole closer to the surface and reduce the effective radius of curvature through gravitational bending of photon orbits. Decreasing the radius of curvature to  $R_*$  allows almost all pulsars to generate sufficient pairs, as shown in Figure 6. Any increase in the effective surface field would produce similar results, when combined with the effects of gravitational bending of the photon orbits (J. Arons, in preparation).

For a conservative model of a self-heated polar cap, the predicted final pair multiplicity is shown in Figure 7. If ICS photons create the PFF, the typical multiplicity is low, in the range of 1–100 for the bulk of pulsars, much lower than the  $10^3$  commonly assumed. If curvature photons stop the acceleration, however, such high multiplicities can be reached.

Since the calculation of the expected multiplicity includes the decay of the magnetic field with distance, the multiplicity gives a good estimate of which pulsars can form the PFF, as discussed in Section 5.5. The total multiplicity shows a steady decline with timing age, dropping to 0.1 near  $10^7$  years, below which the pair creation is too sparse to form the PFF.

In Figure 8, we show the pair multiplicity using the Tsuruta temperature model and no cap heating. The increased stellar temperature keeps the pair multiplicity expected due to NRICS between 10–100 out to a few tens of million years, while the lack of polar cap heating results in curvature dominance and correspondingly high multiplicities for some of the youngest pulsars. If polar cap heating were included, NRICS would truncate beam acceleration for most of those pulsars, dropping the multiplicity back to the 100 – 1000 range.

## 7. CONCLUSIONS

Even without considering the competition between the various emission processes, the most robust result of this work is that most pulsars can generate enough pairs to short out the starvation electric field without invoking a complex dipole structure, if the polar cap temperature is over  $10^6$  K. However, without additional heating, the surface temperature drops below this value after c.  $10^6$  years, making older pulsars problematic. For the hotter stars, nonresonant inverse Compton scattering easily creates pairs in the simple dipole case, unlike the earlier models of pure-curvature cascades (Arons & Scharlemann 1979). Like any cooling neutron star, pulsars should produce observable thermal X-rays, with some enhancement due to the small, but hot, polar cap.

Due to the effects of ICS, the expected pair multiplicities are lower than those expected from curvature cascades, in the range of 1–100, in contrast to the multiplicities of  $10^3$  or higher produced by curvature cascades. Despite the increase of the ICS cross-sections at low energy, the primary beam of particles extracted from the pulsar still accelerates to Lorentz factors of  $10^4$  or higher, due to the lag between the emission of pair-producing photons and their actual conversion into pairs.

The improved death line calculations reveal a regime of pair-production available at high magnetic fields and large periods, first predicted by Arons (1998). At large periods,

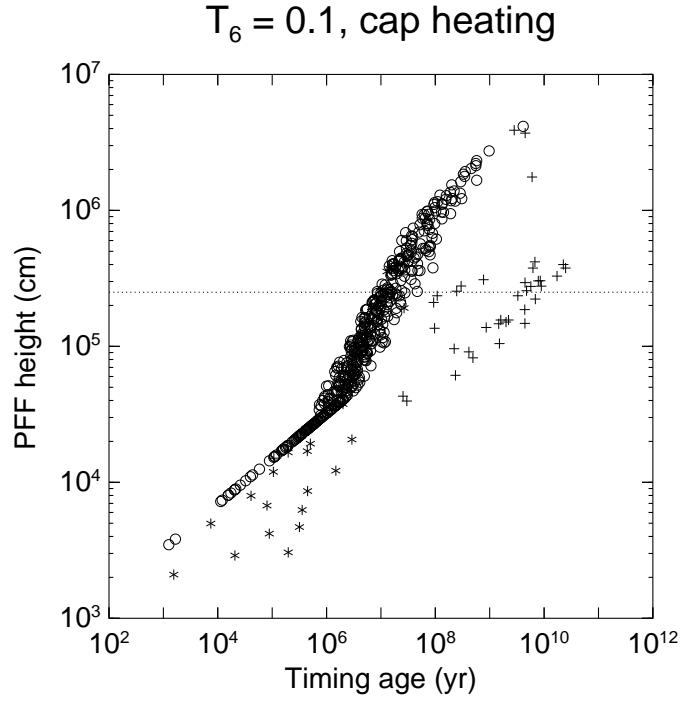


FIG. 4.— PFF height vs. timing age, using a self-consistent hot polar cap. Pulsars dominated by NRICS are marked with circles, those dominated by RICS are marked with stars, and those dominated by curvature are marked with crosses. Above the dotted line at  $s_{PFF} = 0.25 R_*$ , polar-cap NRICS fails to create sufficient pairs to halt acceleration.

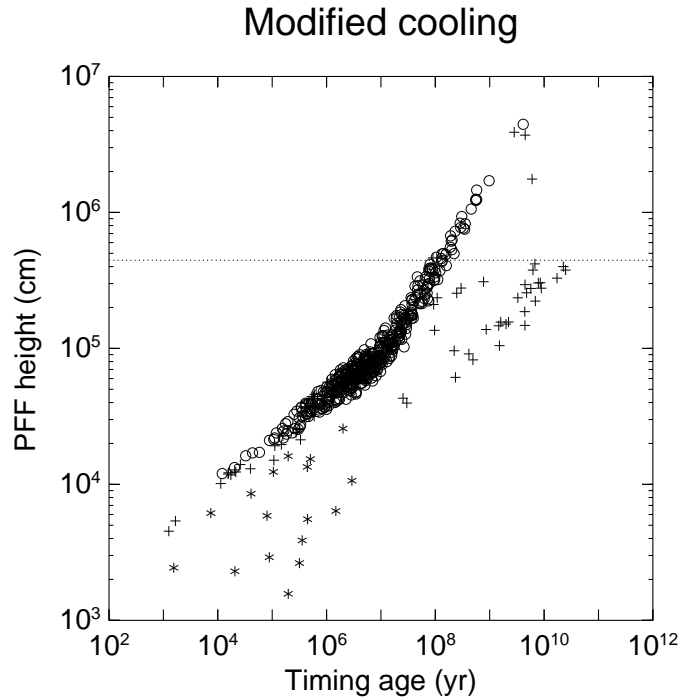


FIG. 5.— PFF height vs. timing age, using a temperature model derived from the magnetic cooling results of Tsuruta (1998). Pulsars dominated by NRICS are marked with circles, those dominated by RICS are marked with stars, and those dominated by curvature are marked with crosses. Above the dotted line at  $s_{PFF} = 0.45 R_*$ , NRICS fails to create sufficient pairs to halt acceleration.

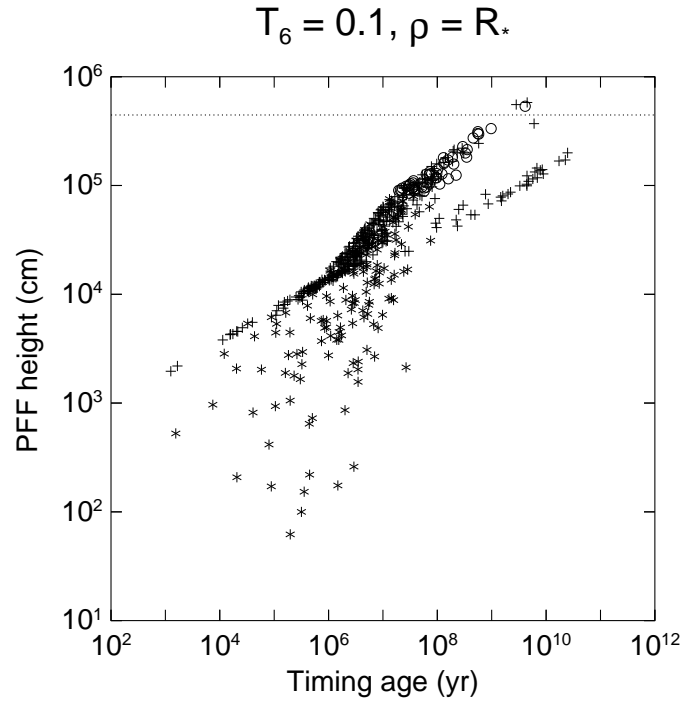


FIG. 6.— PFF height vs. timing age, assuming a modified magnetic field such that the field line radius of curvature is  $10^6$  cm. Pulsars dominated by NRICS are marked with circles, those dominated by RICS are marked with stars, and those dominated by curvature are marked with crosses. Above the dotted line at  $s_{PFF} = 0.45 R_*$ , NRICS fails to create sufficient pairs to halt acceleration.

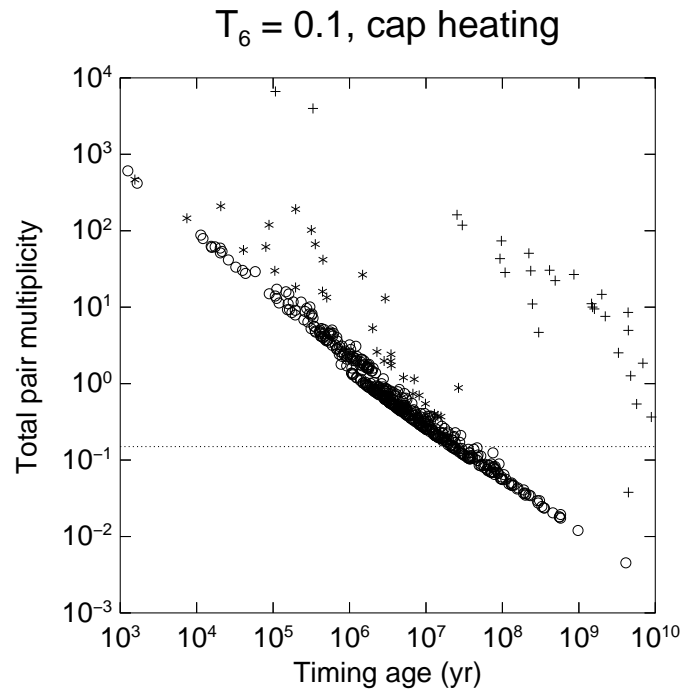


FIG. 7.— Final pair multiplicity,  $\kappa$ , using a self-consistent hot polar cap. Pulsars dominated by NRICS are marked with circles, those dominated by RICS are marked with stars, and those dominated by curvature are marked with crosses.

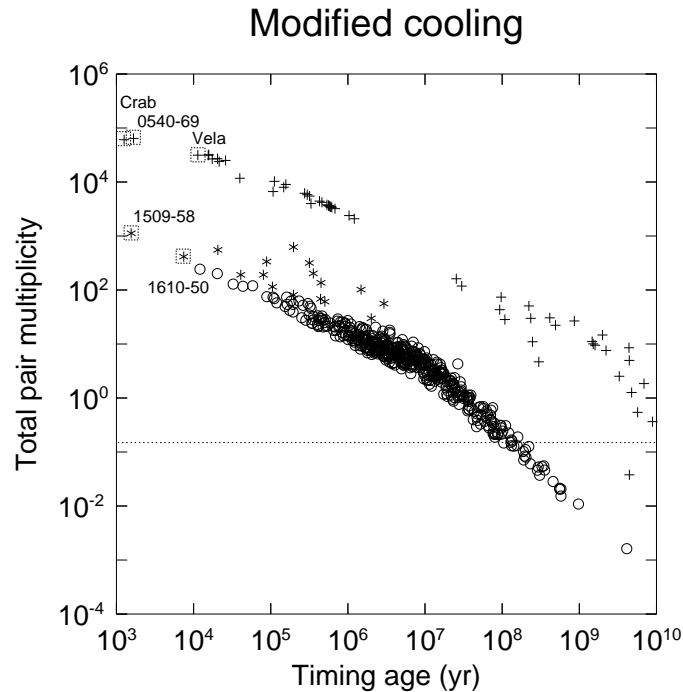


FIG. 8.— Final pair multiplicity,  $\kappa$ , using a temperature model derived from the magnetic cooling results of Tsuruta (1998). Pulsars dominated by NRICS are marked with circles, those dominated by RICS are marked with stars, and those dominated by curvature are marked with crosses. The youngest five pulsars are explicitly labelled.

the polar cap is small and the accelerating electric field weak. The small cap prevents NRICS from producing enough pairs, if only the cap is hot, but the slow acceleration allows RICS to do so easily. The small polar cap also produces a narrow beam, making these objects difficult to detect. The recent discovery of PSR J2144-3933 by Young, et al. (1999) appears to confirm these results, as does the more recent theoretical treatment by Zhang, et al. (2000), which should encourage further searches in this region of parameter space.

Since each of the different emission processes dominates in different regimes of pulsar space, the radio emission process must be insensitive to the precise way in which

the pair plasma was formed. The comparatively low pair-production multiplicities found constrain the radio emission process by limiting the available particle densities.

More detailed studies are, of course, required to understand the expected pair and gamma-ray spectra from these stars. For any given pulsar, more precise calculations are required to compute the beam  $\gamma$  and the PFF height as functions of distance from the magnetic axis, but the general trends illuminated here should hold.

Our research on pulsars was supported in part by NSF grant AST 9528271 and NASA grant NAG 5-3073, and in part by the generosity of California's taxpayers.

#### REFERENCES

- Arons, J., & Scharlemann, E. T. 1979, *ApJ*, 231, 854  
Arons, J. 1981, *ApJ*, 248, 1099  
Arons, J. 1998, in *Neutron Stars and Pulsars*, ed. N. Shibasaki, et al. (Tokyo: Universal Academy Press, Inc.), 339  
Arons, J. 1999, in *ASP Conf. Ser. 201, Pulsar astronomy: 2000 and beyond*: IAU Colloq. 177, ed. M. Kramer, N. Wex, & R. Wielebinski (San Francisco: ASP), 449  
Blumenthal, G. R., & Gould, R. J. 1970, *Reviews of Modern Physics*, 42, 237  
Daugherty, J. K., & Harding, A. K. 1983, *ApJ*, 273, 761  
Dermer, C. D. 1990, *ApJ*, 360, 197  
Gallant, Y. A. & Arons, J. 1994, *ApJ*, 435, 230  
Goldreich, P., & Julian, W. H. 1969, *ApJ*, 157, 869  
Gonthier, P. L., & Harding, A. K. 1994, *ApJ*, 425, 767  
Harding, A. K., Baring, M. G., & Gonthier, P. L. 1997, *ApJ*, 476, 246  
Harding, A. K., & Muslimov, A. G. 1998, *ApJ*, 508, 328  
Hester, J. J., et al. 1995, *ApJ*, 448, 240  
Jackson, J.D. 1975, *Classical Electrodynamics* (2d ed.; New York: John Wiley & Sons, Inc.)  
Kennel, C. F. & Coroniti, F. V. 1984, *ApJ*, 283, 694  
Kramer, M., Xilouris, K. M., Lorimer, D. R., Doroshenko, O., et al. 1998, *ApJ*, 501, 270  
Luo, Q. 1996, *ApJ*, 468, 338  
Luo, Q., & Protheroe, R. J. 1998, *Publications of the Astronomical Society of Australia*, 15, 222  
Lyubarskii, Y. E., & Petrova, S. A. 2000, *A&A*, 335, 406  
Lyne, A. G., & Manchester, R. N. 1988, *MNRAS*, 234, 477  
Muslimov, A. G., & Tsygan, A. I. 1990, *AZh*, 67, 263  
Muslimov, A. G., & Tsygan, A. I. 1992, *MNRAS*, 255, 61  
Muslimov, A. G., & Harding, A. K. 1997, *ApJ*, 485, 735  
Radhakrishnan, V., & Cooke, D. J. 1969, *Astrophys. Lett.*, 3, 225  
Rees, M. J. & Gunn, J. E. 1974, *ApJ*, 167, 1  
Ruderman, M. A., & Sutherland, P. G. 1973, *ApJ*, 196, 51  
Sturrock, P. A. 1971, *ApJ*, 164, 529  
Sturmer, S. J., Dermer, C. D., & Michel, F. C. 1995, *ApJ*, 445, 736  
Sturmer, S. J. 1995, *ApJ*, 446, 292  
Tademaru, E. 1973, *ApJ*, 183, 625  
Taylor, J. H., Manchester, R. N., & Lyne, A. G. 1993, *ApJS*, 88, 529  
Tsuruta, S. 1998, *Phys. Rep.*, 292, 1  
Young, M. D., Manchester, R. N., & Johnston, S. 1999, *Nature*, 400, 848  
Zhang, B., Qiao, G. J., Lin, W. P. & Han, J. L. 1997, *ApJ*, 478, 313  
Zhang, B., Qiao, G. J., & Han, J. L. 1997, *ApJ*, 491, 891  
Zhang, B., Harding, A. K., & Muslimov, A. G. 2000, *ApJ*, 531, L135  
Zhang, B., & Harding, A. K. 2000, *ApJ*, 532, 1150